JOURNAL OF Materials CHEMISTRY

New layered double hydroxides with the hydrotalcite structure containing Ni(II) and V(III)

Francisco M. Labajos, M. Dolores Sastre, Raquel Trujillano and Vicente Rives*

Departamento de Química Inorgánica, Universidad de Salamanca, Salamanca, Spain. Fax +34 923 29 45 74. E-mail: vrives@gugu.usal.es

Received 3rd November 1998, Accepted 14th January 1999

Layered double hydroxides (LDH) with the hydrotalcite-like structure, but containing Ni(II) and V(III) cations in the layers, have been prepared by the constant pH method. Characterization by elemental chemical analysis, powder X-ray diffraction, differential thermal analysis, thermogravimetric analysis, FT-IR spectroscopy, temperature-programmed reduction and specific surface area assessment indicates the formation of well crystallized materials after hydrothermal treatment, without significant oxidation of V(III) species, and with interlayer, flat-oriented, carbonate anions. Reduction in H_2 takes place in a single step at *ca.* 400 °C [Ni(II)→Ni(0)]; V(III) is not reduced. On calcination in air, $Ni_2V_3O_8$ is formed, together with NiO, but crystallization is only evident after calcination at 750 °C. No major difference was found between samples with Ni : V molar ratios close to 2 or 4.

Introduction

Layered double hydroxides (LDHs) with the so-called 'hydrotalcite-like' structure consist of brucite, $Mg(OH)_2$, layers, where a partial M(II)/M(III) substitution gives rise to positively charged layers, balanced by anions,[1] coexisting with water molecules in the interlayer region. Pillaring of these layers gives rise to different polytypes. The general formula is $[M^{II}_{1-x}M^{III}_{x}(OH)_2]$ $(A^{m-})_{x/m}\cdot nH_2O$. The materials display ionic exchange ability, adsorption and catalytic properties, and deserve much attention in recent years because of their use as catalyst precursors. In hydrotalcite-like materials, the cations are rather close to one other, and so, upon calcination they usually lead to homogeneously dispersed mixed oxides with large specific surface areas.[1–3]

Hydrotalcites have been prepared with all first row transition metal cations except Ti(III). On the other hand, decomposition of hydrotalcites with interlayer metal-containing anions (*e.g.*, oxometalates, cyano complexes, halogen complexes, *etc.*)[4] also gives rise to mixed oxides, and represents an alternative route to the preparation of oxides with different cations. It has also been demonstrated that the precise nature of the phases formed upon decomposition changes if a given cation is located in the layers or in the interlayers, *e.g.*, V(III) in the layers or $V_{10}O_{28}^{6-}$ in the interlayers.[5]

In recent years we have reported on the preparation and characterization of different hydrotalcite-like materials, with different cations in the brucite-like layers, and, in some cases, with interlayer metal-containing compounds (oxometalates). In the present paper, we report on the preparation and characterization of hydrotalcites containing Ni(II) and V(III) in the layers. Ni(II) had been previously combined with Al(III)[2] and some other trivalent cations, such as Mn,[6] Cr,[7,8] and Fe,[9–11] and V(III) with Mg(II),[5,12–14] but, to the authors' knowledge, this is the first report on hydrotalcites with these two cations in the brucite-like layers.

As mentioned above, calcination of hydrotalcites gives rise to formation of mixed oxides. For the materials studied here, the formation of $Ni_3(VO_4)_2$, which is isostructural with $Mg_3V_2O_8$,[15] consisting of $[NiO_6]$ octahedra linked to $[VO_4]$ tetrahedra,[16] is expected. Magnesium vanadates are currently used as oxidative dehydrogenation catalysts, and it is expected that Mg/Ni exchange would give rise to changes in surface acidity, thus changing the catalytic properties, as already reported for Ni–Al–V, Ni–Cr–V, and Mg–Cr–V mixed oxides obtained upon calcination of hydrotalcites containing interlayer decavanadate,[17] while it has also been reported[18,19] that nickel vanadates can host intercalated Li ions for use in solid state batteries.

Experimental

Sample preparation

All chemicals used were from Fluka (Switzerland), and gases were from L'Air Liquide (Spain). Two samples, A0 and B0, were prepared, with different nominal Ni/V ratios (see Table 1). Syntheses were carried out following the constant pH method described by Reichle *et al.*[20,21] using Schlenk methods to work under an inert atmosphere.[22] A solution (200 ml) containing V(III) and Ni(II) chlorides in the selected ratio was slowly added to 250 ml of a solution containing 0.14 mol Na_2CO_3 and 0.42 mol NaOH, under similar conditions to those previously described to prepare analogous Mg(II)–V(III) hydrotalcites.[5,12,13] The precipitates obtained were hydrothermally treated at autogenous pressure at 125 °C for 7 (samples A1 and B1) or 14 days (samples A2 and B2) in stainless steel Phaxe 2000 bombs lined with Teflon. In all six cases, the solid was centrifuged and washed until total removal of Na^+ and Cl^- [23] and dried in a desiccator with $CaCl_2$.

Characterisation

Elemental chemical analyses for nickel and vanadium were carried out by atomic absorption in a Mark-2 ELL-240 apparatus at Servicio General de Análisis Químico Aplicado (University of Salamanca, Spain).

The powder X-ray diffraction (PXRD) patterns were recorded in a Siemens D-500 diffractometer equipped with

Table 1 Elemental chemical analysis results and formulae of the samples

Sample	Ni[a]	V[a]	Ni/V[b]	Formula[c]
A0	34.51	12.24	2.45	$[Ni_{0.71}V_{0.29}(OH)_2](CO_3)_{0.15}\cdot 0.92H_2O$
A1	36.27	12.37	2.54	$[Ni_{0.72}V_{0.28}(OH)_2](CO_3)_{0.14}\cdot 0.72H_2O$
A2	36.80	12.17	2.63	$[Ni_{0.72}V_{0.28}(OH)_2](CO_3)_{0.14}\cdot 0.58H_2O$
B0	35.87	7.75	4.02	$[Ni_{0.80}V_{0.20}(OH)_2](CO_3)_{0.10}\cdot 0.89H_2O$
B1	36.29	7.26	4.35	$[Ni_{0.81}V_{0.19}(OH)_2](CO_3)_{0.10}\cdot 0.84H_2O$
B2	38.85	7.43	4.53	$[Ni_{0.82}V_{0.18}(OH)_2](CO_3)_{0.09}\cdot 0.96H_2O$

[a]% weight. [b]Molar ratio. [c]Values have been rounded to the closest 0.01.

Diffract-AT software and a DACO-MP microprocessor, copper ($\lambda = 1.5405$ Å) tube and graphite filter. The crystalline phases were identified from comparison with JCPDS databases.

Differential thermal analyses (DTA) and thermogravimetric (TG) analyses were carried out in Perkin-Elmer DTA 1700 and Perkin-Elmer TGS-2 instruments, respectively, coupled to a Perkin-Elmer 3600 data station. The analyses were carried out under a flow of air or nitrogen (60 ml min^{-1}) at a heating rate of 12 °C min^{-1}.

The FT-IR spectra were recorded following the KBr pellet technique in a Perkin-Elmer FTIR-1730 spectrometer, with a nominal resolution of 4 cm^{-1} and averaging 100 scans to improve the signal-to-noise ratio.

The nitrogen adsorption–desorption isotherms for specific surface area and porosity assessment were recorded at −196 °C in a Gemini instrument from Micromeritics, after degassing the samples for 2 h at 150 °C in a Flowprep 060 apparatus, also from Micromeritics; the isotherms were analyzed using literature software.[24]

Temperature-programmed reduction (TPR) runs were performed in a TPR/TPD 2900 instrument from Micromeritics, using a 5% H_2/Ar (by volume) mixture to reduce the samples. Amounts of samples of *ca.* 15 mg were used, and the gas flow, sample weight and heating rate (10 °C min^{-1}) were chosen in order to attain good resolution of the reduction peaks.[25] The gas, at the reactor exit, was passed through a cold trap (melting isopropanol) to retain vapours and condensable gases before entering the detector.

Results and discussion

Hydrotalcites

All samples were green, their intensity depending on the Ni content. Chemical analysis results are summarized in Table 1; the formulae, also included in Table 1, were determined assuming carbonate as the single anion in the interlayer (FT-IR results below), while the water contents were calculated from TG measurements (see below). The Ni/V ratios in the solids obtained are slightly larger than those in the starting solutions; this sort of disagreement is usually found when synthesizing LDHs.[3] Upon hydrothermal treatment, the ratio steadily increases, indicating that some changes take place in the solids; this treatment also leads to higher crystalline solids (see PXRD results below), as concluded from sharper and more intense diffraction peaks for samples X1 and X2 than for samples X0. The ionic radii of Ni(II) and V(III) in octahedral coordination (*i.e.*, that attained in the $M(OH)_6$ units of the brucite-like layers) are 0.83 and 0.78 Å, respectively.[26] Substitution consequently leads to some sort of distortion and, probably, under hydrothermal treatment, removal of distorting V(III) cations is favoured.

The water content in the interlayer is within the expected values for this sort of material. Assuming a close packing of carbonate and water molecules in the interlayer, and assuming that the size of an oxide ion is the same as that of a water molecule, and one third of a carbonate anion, the maximum number of water molecules in the interlayer, per 'formula' of hydrotalcite-like material ($[M^{II}_{1-x}M^{III}_{x}(OH)_2](CO_3)_{x/2}\cdot nH_2O$) would be $n \leqslant 2-3x/2$.[27] The experimental values (see Table 1) are always lower than the maximum expected value, probably because of preferred orientation of the interlayer species, due to hydrogen bonding.

Powder X-ray diffraction patterns for all six samples are included in Fig. 1. Ascription of the peaks recorded to diffraction planes was done assuming a 3R packing of the layers[28,29] and the *a* and *c* values calculated as follows. In this packing, the spacing corresponding to the first harmonic, planes (003), at low 2θ values corresponds to one third of the *c* dimension,

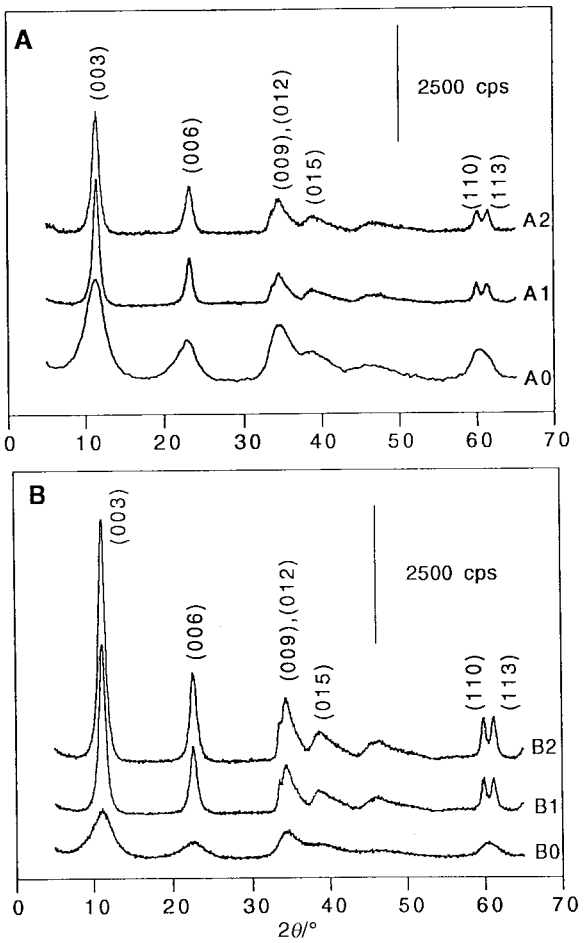

Fig. 1 PXRD patterns for the samples studied.

and the second harmonic, planes (006), to one sixth of such a value. If the peaks are sharp enough, determination of *c* is performed from the position of any of them; however, as the peaks are somewhat broad, dimension *c* has been calculated averaging both positions, according to:

$$c = (3/2)\,[d_{(003)} + 2\,d_{(006)}]$$

On the other hand, the value of *a*, corresponding to the average cation–cation distance in the brucite-like layers, is related to the position of the peak due to planes (110), the first (low 2θ) of the doublet recorded close to $2\theta = 60°$, by:

$$a = 2\,d_{(110)}$$

The values calculated for *a* and *c* for all six samples are included in Table 2, together with the experimental and calculated (assuming 3R packing) positions of the main maxima recorded, and with JCPDS data for hydrotalcite. The value of lattice constant *a* slightly increases for the samples submitted to hydrothermal treatment, if compared to those for the parent samples; this could be due to the progressive removal of V(III) from the brucite-like layers (leading to larger Ni/V ratios), and following Vegard's rule, *a* increases as the content of Ni(II), with a larger ionic radius, increases; nevertheless, the variation is extremely small, and the values are almost coincident for both series of samples. On the other hand, when comparing the values for parameter *c*, it is observed that, for a given series of samples (A or B), it decreases as the Ni(II) content does, although, if the value of *c* were related to the ionic radii of the cations in the brucite-like layers, the opposite effect would be observed; the *c* value for a series B sample is always larger than that for the corresponding series A sample. This may be related to the different Ni(II)/V(III) ratio. As the content of the trivalent cation decreases, the formal positive

Table 2 Calculated and experimental spacings (Å) for main diffraction maxima of the samples, their ascription, values for hydrotalcite from JCPDS file 14-191 (HT), and lattice parameters a and c (Å)

A0		A1		A2		B0		B1		B2			
d_{exp}	d_{calc}	d_{exp}	d_{calc}	d_{exp}	d_{calc}	d_{exp}	d_{calc}	d_{exp}	d_{calc}	d_{exp}	d_{calc}	(hkl)	HT
7.79	7.79	7.67	7.67	7.65	7.65	7.95	7.95	7.89	7.89	7.86	7.86	(003)	7.69
3.88	3.90	3.82	3.84	3.81	3.83	3.92	3.98	3.92	3.95	3.90	3.93	(006)	3.88
2.59	2.60	2.60	2.56	2.60	2.55	2.58	2.65	2.60	2.63	2.60	2.62	(009)	2.58
2.59	2.58	2.60	2.60	2.60	2.60	2.58	2.59	2.60	2.60	2.60	2.60	(012)	2.58
2.32	2.31	2.32	2.31	2.31	2.31	2.34	2.32	2.34	2.32	2.32	2.32	(015)	2.30
1.98	1.96	1.90	1.96	1.94	1.95	1.93	1.98	1.96	1.98	1.94	1.98	(018)	1.96
1.53	1.53	1.54	1.54	1.54	1.54	1.53	1.53	1.54	1.54	1.54	1.54	(110)	1.53
		1.51	1.51	1.51	1.51	1.43	1.50	1.52	1.51	1.51	1.51	(113)	1.50
23.31[a]		22.97		22.91		23.84		23.75		23.49			23.07
3.06[b]		3.08		3.08		3.06		3.08		3.08			3.06

[a]Lattice parameter c. [b]Lattice parameter a.

charge of the layers decreases as well, and thus the electrostatic forces between the layers and the interlayer anions, therefore increasing the spacing (value for series B larger than for series A).[2,30] The differences among the samples within a given series should be related to the changes introduced by the hydrothermal treatment, probably a better packing of the layers.

The PXRD peaks become sharper and more intense upon submitting the samples to hydrothermal treatment; we have previously shown[7,30] that this effect is important for treatments shorter than 7 days, becoming less evident when the hydrothermal treatment is prolonged. The lack of symmetry of the peaks due to (hkl) planes with $h \neq 0$ and $k \neq 0$ is probably due to a turbostatic disorder between the layers.

Differential thermal analysis curves for selected samples are shown in Fig. 2. As the samples contain oxidizable cations, the analyses were recorded both in nitrogen (inert) and in oxygen (oxidant). The curves recorded for sample A0 (in nitrogen) and for sample B0 (both in nitrogen and in air) are coincident with those reported[8,31,32] for this sort of material, with a first endothermic peak around 130 °C, associated with removal of interlayer water molecules, and a second peak at *ca.* 330 °C, due to removal of layer hydroxyls (condensed to water molecules) and interlayer carbonate anions (as CO_2). However, the curve recorded for sample A0 in air is completely different and, after the first endothermic peak, an ill-defined, broad endothermic peak is recorded. This behaviour is undoubtedly related to the presence of oxidizable cations, V(III), in the sample. During calcination in air, the V(III) ions are oxidized, an exothermic process which presumably takes place in the same temperature range as the endothermic removal of water and CO_2; consequently, both effects become almost completely cancelled. In the case of sample B0, however, the exothermic effect seems to be absent, probably because the amount of heat released during oxidation is sensibly smaller than in the case of sample A0, due to the much lower V(III) content in sample B0. When comparing samples B0 and B2, Fig. 2, it can be observed that while the second endothermic effect seems to be about the same in both cases, the first endothermic effect is much sharper for sample B2 than for sample B0. Probably, hydrothermal treatment has led to a higher crystallinity of the samples, decreasing the temperature range for water removal.

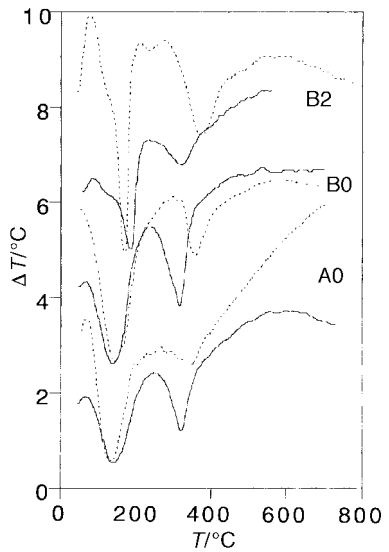

Fig. 2 Differential thermal analysis and thermogravimetric analysis curves for selected samples. The diagrams were recorded in air (dotted line) and in nitrogen (solid line).

These conclusions coincide with those which can be obtained from the TG results; the curves for the original samples (A0 and B0) are included in Fig. 3. In all cases, two consecutive weight losses are recorded, the inflexion points of which roughly coincide with the minima of the DTA curves, and so a correlation can be established between the thermal effects giving rise to these curves; weight losses are observed at slightly lower temperatures when the analysis is carried out in nitrogen than when it is carried out in air.

It should be noted that, for sample A0, the weight loss recorded in air is lower than when the pattern is recorded in nitrogen. This difference comes from the oxidation process, V(III)→V(V), taking place in air. Upon heating and decomposition, hydrotalcites give rise to mixed oxides. From a Mg,Al-CO_3 hydrotalcite, MgO and $MgAl_2O_4$ are formed;[30,33,34] from a MgV-CO_3 hydrotalcite, MgO and V_2O_3 (or solids related to these) will be formed in nitrogen, but MgO and V_2O_5 in oxygen, thus accounting for the larger weight in air of the

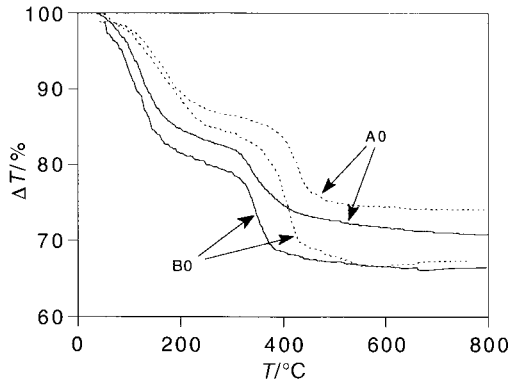

Fig. 3 Thermogravimetric analysis curves for parent samples. The diagrams were recorded in air (dotted line) and in nitrogen (solid line).

final solid, *i.e.*, a lower weight loss. The fact that sample B0 gives rise to a total weight loss coinciding (within experimental error) in air and in nitrogen can be explained by taking into account that the extremely small vanadium content in this sample makes it difficult to distinguish any difference in the weight of the solid obtained after heating.

As the first weight loss is attributed to removal of interlayer water molecules,[35,36] their determination can be straightforwardly carried out; the values obtained are included in Table 1.

FT-IR spectroscopy was applied in order to confirm the nature of the interlayer anion; it is well known that carbonate is strongly held in the interlayer space of hydrotalcites[37,38] and that polyvalent anions are hosted in preference to monovalent ones; thus, intercalation of carbonate, rather than nitrate, is expected. On the other hand, formation of crystals where two different sorts of anion coexist in the interlayer space is strongly unstable,[3] and so if two different anions, with different molecular size and/or orientation in the interlayer space, exist in the interlayer, two series of high order reflections are usually recorded in the PXRD diagrams.[39]

The spectra for samples A1 and B1 are shown in Fig. 4; no major differences were found for samples A2 and B2, while for samples A0 and B0 the bands recorded were slightly broader. The broad band around 3400 cm^{-1} is due to OH stretching of hydrogen-bonded hydroxyl groups and water molecules. Note the extreme broadness of this band on the low wavenumber side, which is probably due to the presence of a weak shoulder around 3200 cm^{-1}, which was previously ascribed to the OH stretching mode of water molecules hydrogen bonded to interlayer carbonate anions.[27,35,40] The group of weak bands around 2928 cm^{-1} are due to ν_{C-H} modes of adsorbed organic impurities, while the weak feature at 2354 cm^{-1} is due to a miscancellation of the bands due to gaseous CO_2 during recording of the spectra of the sample and the background. The band close to 1635 cm^{-1} is originated by the bending mode of interlayer water molecules.

Most of the bands in the low wavenumber region (below 1000 cm^{-1}) are due to metal–oxygen vibration modes and their assignment is rather complicated, taking into account the similarity between the atomic weights of Ni and V. The remaining absorptions are mostly due to carbonate modes. The band at 1366 ± 5 cm^{-1}, with a weak shoulder at *ca.* 1482 cm^{-1} in sample B1, comes from splitting of the band due to the ν_3 mode of carbonate. Although this band is recorded at 1450 cm^{-1} for free carbonate, it shifts and splits as the symmetry (D_{3h} in free carbonate) is decreased; the cases of calcite (symmetry D_3, band at 1492–1429 cm^{-1}) and aragonite (symmetry C_s, bands at 1502 and 1492 cm^{-1}) are well documented in the literature.[41,42] Such a shift has already been reported for other carbonate-containing hydrotalcites.[40] Larger deviations have been reported recently for Mg,Al,Y hydrotalcites,[43] where, in addition to a decrease in the local symmetry of the carbonate anion in the interlayer, electrostatic interactions should arise from the heavy distortion of the brucite-like layers due to the different sizes of the cations. Correspondingly, activation of the totally symmetric mode, ν_1, slightly above 1000 cm^{-1}, is observed in both cases, Fig. 4. Other bands due to carbonate are recorded at lower wavenumbers. In any case, the bands due to carbonate are sharper and stronger in series B samples than in series A ones; probably, the lower carbonate contents permit in some way a more symmetric disposition of the carbonate anions in the interlayer.

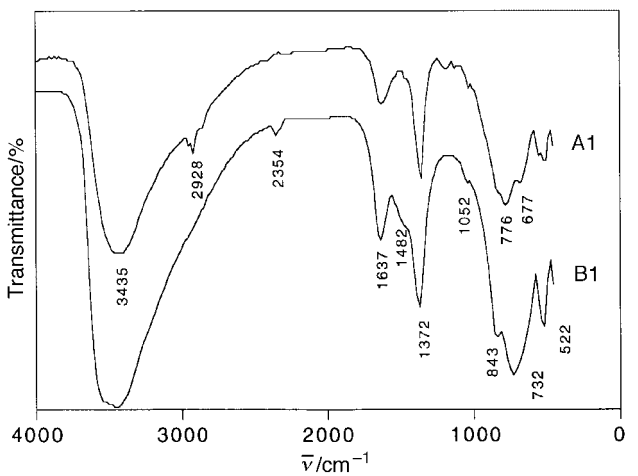

Fig. 4 FT-IR spectra for samples A1 and B1.

Temperature-programmed reduction (TPR) curves were rather similar for all six samples; those for samples A1 and B1 are shown in Fig. 5. From previous TPR studies on hydrotalcites[44] it was concluded that under the experimental conditions used, Ni(II) ions are reduced to the zero-valent state, while V(III) ions are not reduced; carbonate is removed instead of being reduced to C or hydrocarbons. So, the single, although asymmetric, peak recorded in both cases at *ca.* 400 °C should be due to reduction of Ni(II), which takes place with a nominal H_2/Ni consumed molar ratio of 1.0. In these samples, the experimental ratios, as calculated from the nickel content obtained by elemental chemical analysis (Table 1) and hydrogen consumption (related to the area under the recorded curve), were 1.08 and 1.06, respectively, for samples A1 and B1, thus confirming reduction of Ni(II). Although the difference from the expected value is within experimental error, a partial oxidation of V ions close to the particle borders would account for the values being larger than unity.

The nitrogen adsorption–desorption isotherms were recorded at −196 °C. Those for samples A1 and B1 are shown in Fig. 6. Both correspond to type II in the IUPAC classification,[45] although a type H4 hysteresis loop is recorded for sample A1; this shape corresponds to the presence of slit-like mesopores, formed by plate-like particles. Although the nitrogen molecules are not small enough to enter in the interlayer space (and swelling of the structure is not expected, due to the non-polar nature of the N_2 molecule, and the low temperature at which adsorption is measured), probably the primary

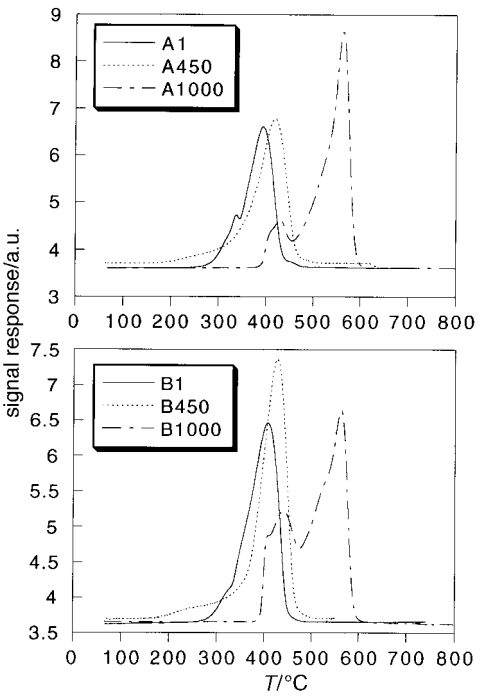

Fig. 5 TPR profiles for samples A1, B1, A-450, B-450, A-1000, and B-1000.

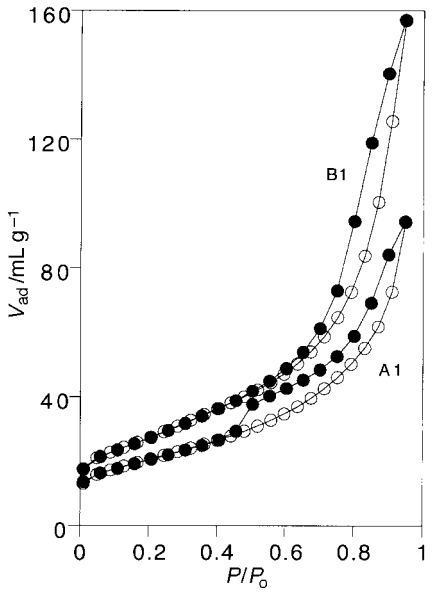

Fig. 6 Nitrogen adsorption–desorption isotherms for samples A1 and B1.

particles are associated in plates. The curve recorded for sample B1, also corresponding to type II, shows, however, a narrow hysteresis loop, corresponding to type H3, ascribed to mesopores open at both ends, probably slit-like pores in these samples. The specific surface areas calculated were 72 $m^2 g^{-1}$ for sample A1, and 97 $m^2 g^{-1}$ for sample B1; similar values were obtained for samples A2 and B2, and the samples did not contain micropores, as concluded from the *t*-plots.[46] Adsorption abilities of samples A1 and A2 were similar, as those of samples B1 and B2, as confirmed from the *f*-plots.[47]

Calcined products

As it is well known, one of the most interesting uses of hydrotalcites and related materials is as precursor for preparation of well dispersed mixed oxides. As cations in the hydrotalcite are homogeneously located in the brucite-like layers, upon calcination they lead to phases where such a homogeneous dispersion is preserved. However, it is difficult to obtain pure phases, because the M(II)/M(III) ratio in hydrotalcites is different to that existing in spinels. According to data in the literature,[2] such a ratio should be between 2 and 5 to avoid coprecipitation, when synthesizing the hydrotalcite, of the corresponding $M(OH)_3$ or $M(OH)_2$ hydroxides. Calcination of a M(II)–M(III) hydrotalcite (without oxidizable cations) thus leads to a mixture of $M^{II}O$ and $M^{II}M^{III}{}_2O_4$.[48,49] However, if oxidizable cations exist, other products can be formed,[5] due to simultaneous decomposition and oxidation. In the present study, we calcined samples A1 and B1 (better crystallized than samples A0 and B0) in air for 2 h at temperatures selected from the DTA curve. The temperatures chosen were 150, 250, 300, 450, 550, 750, and 1000 °C. The first one corresponds, approximately, to the temperature just after the first endothermic effect, due to removal of interlayer water; the second and third temperatures are just before and at the second effect; 550 °C corresponds to the end of the thermal effects, and, finally, samples calcined at 750 and 1000 °C should be hopefully crystalline enough to determine unambiguously the phases present. These samples are named as A-*T* (B-*T*), where *T* stands for the calcination temperature, in °C, and have been characterized by PXRD, FT-IR spectroscopy and texture assessment by nitrogen adsorption at −196 °C.

The PXRD diagrams for series B-*T* are shown in Fig. 7. Differences with the behaviour shown by samples A-*T* were

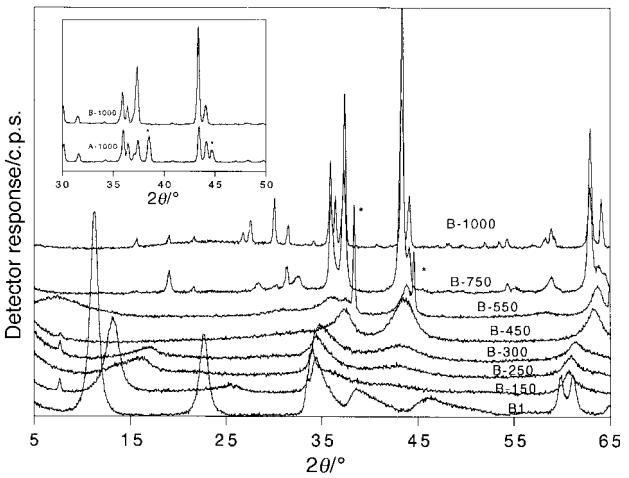

Fig. 7 PXRD patterns for sample B1 calcined at the temperatures given (°C) (* = diffraction peaks due to the A1 sample holder).

only evident after calcination at high temperatures, and will be commented upon below.

Calcination at 150 °C does not destroy the layered structure, as high order reflections due to planes (*h*00) are still recorded, although shifted towards higher 2θ values (lower spacings), probably due to removal of interlayer water molecules; also, these peaks broaden slightly, indicating a decrease in crystallinity. Upon calcination at 250 °C sharp diffraction peaks are no longer recorded, and four broad diffractions are recorded, positions of which coincide with those of the presumably dehydrated sample after calcination at 150 °C. It seems that the layered structure (highly disordered) is stable up to *ca.* 450 °C. Calcination at this temperature, however, leads to a profile with only three broad reflections, the positions of which coincide rather well with those reported in the literature for the rock-salt structure NiO, without any reflection which could be attributed to any V-containing material. This behaviour is not unusual, and in the case of Mg,Al hydrotalcites, crystallization of the spinel, in addition to MgO, is observed only after calcining the samples at temperatures as high as 1000 °C,[30,34] while Al(III) ions are dissolved in the MgO lattice at lower temperatures. This situation gives usually rise to small shifts in the positions of the peaks, with respect to those reported for pure MgO, because of the difference in the ionic radii of Mg(II) and Al(III). In our case, however, the peak recorded at 2.55 Å for the sample calcined at 300 °C is at a higher spacing than the peak due to NiO (2.41 Å), and that at 1.49 Å is recorded also at a higher spacing (1.475 Å for NiO); but the position of the central peak coincides with that reported for NiO (2.09 Å). If the shift were originated by an isomorphic Ni/V substitution, it would be expected that the shift would be in the same direction in all cases (towards larger or towards smaller spacings). These findings mean that the shift is not due to such an isomorphic substitution.

When the calcination temperature is increased to 750 °C, many well defined, sharper peaks are recorded, this finding being more evident after calcination at 1000 °C. It can be easily observed that the new peaks are somewhat 'grouped' in the 2θ ranges where the diffraction peaks due to NiO are recorded. In other words, the broad peaks recorded close to 2.5, 2.1, and 1.5 Å (*ca.* 2θ = 36, 42, and 63°) in the profile of the sample calcined at 450 °C should correspond to diffraction by extremely distorted, ill-crystallized species, which crystallize upon heating at high temperature, thus resolving into sharp, well defined peaks. On comparison with literature reference data, the peaks recorded (both for series A-*T* and for series B-*T*) correspond, in addition to NiO (bunsenite, JCPDS file 4-835), to $Ni_3(VO_4)_2$ (JCPDS file 37-353). It should be noted that, due to the small amount of sample available in some

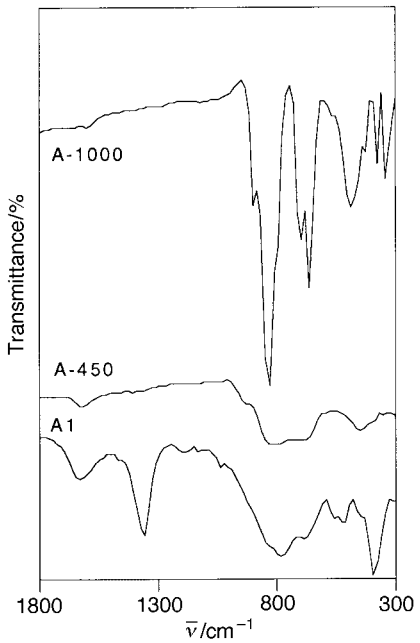

Fig. 8 FT-IR spectra of sample A1 (original) and calcined at 450 and 1000 °C.

cases, Al sample holders were used, and so diffraction peaks due to Al (2.338, 2.022, and 1.432 Å) were recorded, and were used as a sort of 'internal reference'. As mentioned above, $Ni_3(VO_4)_2$ is isostructural with $Mg_3V_2O_8$, and crystallization of $Mg_3V_2O_8$ upon calcination of Mg,V hydrotalcites has been previously reported.[5,13]

No major difference could be observed between the behaviour of samples A-*T* and B-*T*; in both cases mostly amorphous materials were formed at intermediate calcination temperatures, giving rise to crystalline $Ni_3V_2O_8$ and NiO at 750 and 1000 °C. The only difference was in the relative intensities of the diffraction lines due to NiO and $Ni_3V_2O_8$, the former being more intense for series B samples than for series A samples, as expected from the relative amounts of Ni and V in the parent samples (see inset in Fig. 7).

FT-IR spectra for samples A-*T* and B-*T* confirm the conclusion reached from the PXRD study: carbonate is completely removed after calcination at 450 °C, and at 1000 °C bands are recorded below 900 cm^{-1} which can be ascribed to different vibration modes of tetrahedral [VO_4] units (see Fig. 8); the positions of the main bands, as well as their assignments, from comparison with literature data[50] are included in Table 3.

Temperature-programmed reduction (TPR) profiles for samples calcined at 450 °C and 1000 °C are included in Fig. 5. As shown by PXRD data above, calcination at 450 °C leads to mostly amorphous samples (where FTIR data show removal of carbonate), while at 1000 °C crystallization of well defined phases has been completed. Hydrogen consumptions calculated from these curves were larger than those needed for reduction of Ni^{2+} to Ni^0 only, indicating that other reducible species (absent in the uncalcined samples) exist in these samples. The values measured are in agreement with, in addition to reduction of Ni^{2+} to Ni^0, a $V^{5+}\rightarrow V^{3+}$ reduction, *i.e.*, oxidation of V^{3+} has already taken place at 450 °C, in agreement with the DTA profiles recorded in air (see Fig. 2).

Table 3 Positions (cm^{-1}) and assignments of bands recorded in the spectra of samples A1 and B1 calcined at 1000 °C

A-1000	B-1000	Assignment
891	892	$\nu_{as}(VO_4)$
829	828	$\nu_s(VO_4)$
700	702	$\nu_{as}(VOV)$
482	482	$\nu_s(VOV)$
428	428	$\delta_{as}(VO_4)$
339	338	$\delta_s(VO_4)$

However, note also the different shape of the curves as the calcination temperature is increased. For samples calcined at 450 °C a single reduction peak is recorded, at slightly higher temperature than that needed to reduce Ni^{2+} in the original samples. On increasing the calcination temperature to 1000 °C, a double peak is recorded, with a broad maximum at *ca.* 430 °C, and a sharper one at *ca.* 550 °C. Between these two temperatures, shoulders can be also observed; the resolved shoulders in the first maximum for sample B-1000 are probably also present in the reduction profile of sample A-1000, but as in this case the peak is weaker, they can be hardly detected.

The area under the curve corresponds, once normalized and calibrated, to the amount of hydrogen consumed during reduction. In these samples, as two different cations are reduced, and two peaks are recorded (for samples calcined at 1000 °C), it seems easy to ascribe each peak to a reduction process. However, this is not always straightforward.

Elemental chemical analysis for sample A-1000 gives 44.7% Ni and 15.12% V. Assuming NiO and $Ni_3(VO_4)_2$, *i.e.*, the crystalline phases detected by PXRD, are the only phases existing in this sample (and vanadium is acting as a limiting reagent), its formula corresponds to $Ni_3(VO_4)_2{\cdot}2.14NiO$. If reduction of Ni^{2+} (to Ni^0) and V^{5+} (to V^{3+}) takes place in two different steps, the ratio between the integrated areas of the peaks would be 5.14:2, *i.e.*, 2.57:1; otherwise, if each crystalline species is reduced in a single step, then the ratio between the corresponding reduction peaks would be 2.14:1. However, a tentative deconvolution of the two peaks recorded for sample A-1000 indicates a ratio (second peak : first peak) of 6:1. Similar results were obtained for sample B-1000 (44.5% Ni, 9.1% V), with an assumed formula of $Ni_3(VO_4)_2{\cdot}5.5NiO$; so, step-by-step reduction of cations would lead to a ratio between the areas of the peaks of 4.3:1, while if step-by-step reduction of crystalline species takes place, the expected ratio would be 0.9:1; the experimental ratio was 2:1. These results indicate that, unfortunately, no further information can be concluded from the TPR results on the reduction sequence of these materials. Probably, reduction of Ni^{2+} and V^{5+} takes place simultaneously, and the different peaks are a consequence of different reduction kinetics, probably related to different crystallite size, proximity to crystallite edges, *etc.*

The specific surface areas of the samples, as well as their pore volumes, have been measured from the corresponding nitrogen adsorption–desorption isotherms at −196 °C. The changes in these variables with the calcination temperature have been plotted in Fig. 9. As observed previously with other hydrotalcite-like materials,[30,51,52] an increase is observed up

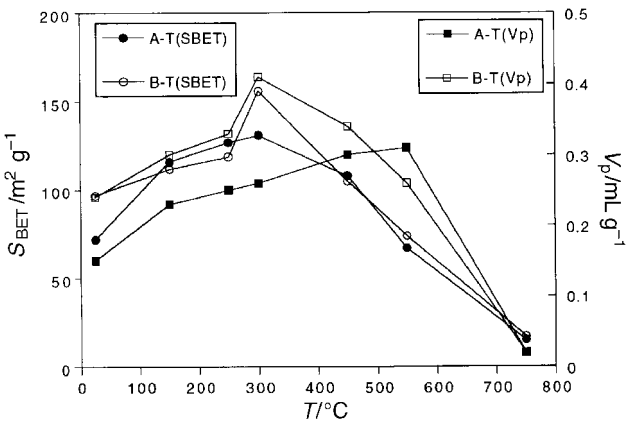

Fig. 9 Changes in specific surface area and pore volume for samples A1 and B1 with the calcination temperature.

to intermediate calcination temperatures, where PXRD data indicate formation of mostly amorphous materials. At higher temperatures, where crystallization of NiO and $Ni_3(VO_4)_2$ takes place, both the specific surface area and the pore volume sharply decrease. Calcination below 550 °C leads to type IV isotherms in the case of the A samples (type II for samples B), due to capillary condensation in mesopores, where adsorption is limited for high relative pressures; the hysteresis loop is characteristic of pores with narrow necks. The width of the hysteresis loop decreases as the calcination temperature is increased, and also in this same sense decreases the adsorption capacity.

When the calcination temperature is increased, the specific surface area decreases, and values close to $5\,m^2\,g^{-1}$ were measured for the samples calcined at 1000 °C. Formation of micropores is also observed at intermediate temperatures, but they represent merely *ca.* 10% of the total surface area.

Pore size distribution curves were also rather similar for both series of samples. A narrow distribution of pore size is observed for the uncalcined solids (*ca.* 4 nm); the maximum shifts towards larger diameters as the calcination temperature is increased, and simultaneously broadens.

Conclusions

The synthesis method followed leads, upon thermal treatment, to well crystallized, single phase, hydrotalcites, with Ni(II) and V(III) in the brucite-like layers, and with interlayer carbonate ions, with their molecular plane parallel to the brucite-like layers. This is the first description in the literature of LDH materials containing simultaneously Ni(II) and V(III). Oxidation of V(III) to higher oxidation states is negligible. On reduction, Ni(II) is reduced to Ni(0) at *ca.* 400 °C, and V(III) is not reduced. Calcination at increasing temperatures leads to destruction of the layered structure and progressive formation of NiO and $Ni_2V_3O_8$, after calcination at 750 °C, this crystallization leading to a sharp decrease in the specific surface area.

Acknowledgements

The authors are grateful for financial support from DGES (grant PB96-1307-C03-01) and Junta de Castilla y León (Consejería de Educación y Cultura, grant SA45/96).

References

1 F. Trifirò and A. Vaccari, in *Comprehensive Supramolecular Chemistry*, ed. J. L. Atwood, J. D. Davies, D. D. MacNicol, F. Vögtle, J.-M. Lehn, G. Alberti and T. Bein, Pergamon-Elsevier Sci. Ltd., Oxford, 1996, vol. 7, p. 251, and references therein.
2 F. Cavani, F. Trifirò and A. Vaccari, *Catal. Today*, 1991, **11**, 173, and references therein.
3 A. de Roy, C. Forano, K. El-Malki and J. P. Besse, in *Expanded Clays and Other Microporous Solids*, ed. M. L. Occelli and H. E. Robson, Van Nostrand Reinhold, New York, 1992, p. 108, and references therein.
4 V. Rives and M. A. Ulibarri, *Coord. Chem. Rev.*, 1999, **181**, 61.
5 F. Kooli, I. Crespo, C. Barriga, M. A. Ulibarri and V. Rives, *J. Mater. Chem.*, 1996, **6**, 1199.
6 C. Barriga, J. M. Fernández, M. A. Ulibarri, F. M. Labajos and V. Rives, *J. Solid State Chem.*, 1996, **124**, 205.
7 F. M. Labajos, Ph. D. Thesis, University of Salamanca (Spain), 1993.
8 F. M. Labajos and V. Rives, *Inorg. Chem.*, 1996, **35**, 5313.
9 E. Uzunova, D. Klissurski and S. Kassabov, *J. Mater. Chem.*, 1994, **4**, 153.
10 R. Trujillano, Ph. D. Thesis, University of Salamanca (Spain), 1997.
11 M. del Arco, P. Malet, R. Trujillano and V. Rives, *Chem. Mater.*, in press.
12 V. Rives, F. M. Labajos, M. A. Ulibarri and P. Malet, *Inorg. Chem.*, 1993, **32**, 5000.
13 F. M. Labajos, V. Rives, P. Malet, M. A. Centeno and M. A. Ulibarri, *Inorg. Chem.*, 1996, **35**, 1154.
14 P. Malet, J. A. Odriozola, F. M. Labajos, V. Rives and M. A. Ulibarri, *Nucl. Instrum. Methods Phys. Res. B*, 1995, **97**, 16.
15 A. Durif, *Anal. Chem.*, 1959, **31**, 1741.
16 N. Krishnamachari and C. Calvo, *Can. J. Chem.*, 1971, **49**, 1629.
17 F. Kooli, C. Martín and V. Rives, *Langmuir*, 1997, **13**, 2303.
18 E. Andrukaitis, *J. Power Sources*, 1997, **68**, 652.
19 A. Manthiram and J. Kim, *Chem. Mater.*, 1998, **10**, 2895.
20 W. T. Reichle, *Solid State Ionics*, 1986, **22**, 135.
21 W. T. Reichle, *Chemtech*, 1986, **16**, 58.
22 D. F. Shriver and M. A. Drezdzon, *The Manipulation of Air-Sensitive Compounds*, 2nd edn., Wiley, New York, 1986.
23 F. Burriel, F. Lucena, S. Arribas and J. Hernández, *Química Analítica Cualitativa,* XIII. edn., Paraninfo, Madrid, 1989.
24 V. Rives, *Adsorption Sci. Technol.*, 1991, **8**, 95.
25 P. Malet and A. Caballero, *J. Chem. Soc., Faraday Trans.*, 1988, **84**, 2369.
26 J. E. Huheey, E. A. Keiter and R. I. Keiter, *Inorganic Chemistry: Principles of Structure and Reactivity*, 4th edn., Harper Collins, New York, 1993.
27 S. Miyata, *Clays Clay Miner.*, 1975, **23**, 369.
28 A. S. Bookin and V. A. Drits, *Clays Clay Miner.*, 1993, **41**, 551.
29 A. S. Bookin, V. I. Cherkashin and A. Drits, *Clays Clay Miner.*, 1993, **41**, 558.
30 F. M. Labajos, V. Rives and M. A. Ulibarri, *J. Mater. Sci.*, 1992, **27**, 1546.
31 L. Pesic, S. Salipurovic, V. Markovic, D. Vucelic, W. Kagunya and W. Jones, *J. Mater. Chem.*, 1992, **2**, 1069.
32 M. del Arco, V. Rives, R. Trujillano and P. Malet, *J. Mater. Chem.*, 1996, **6**, 1419.
33 A. Vaccari and M. Gazzano, *Stud. Surf. Sci. Catal.*, 1995, **91**, 893.
34 T. Sato, H. Fujita, T. Endo, M. Shimada and A. Tsunashima, *React. Solids*, 1988, **5**, 219.
35 D. L. Bish and G. W. Bridley, *Am. Mineral.*, 1977, **62**, 458.
36 W. Kagunya, P. K. Dutta and Z. Lei, *Physica B*, 1997, **234–236**, 910.
37 D. L. Bish, *Bull. Miner.*, 1980, **103**, 170.
38 S. Miyata, *Clays Clay Miner.*, 1983, **31**, 305.
39 I. Crespo, C. Barriga, V. Rives and M. A. Ulibarri, *Solid State Ionics*, 1997, **101–103**, 729.
40 M. J. Hernández-Moreno, M. A. Ulibarri, J. L. Rendón and C. J. Serna, *Phys. Chem. Miner.*, 1985, **12**, 34.
41 K. Nakamoto, *Infrared and Raman Spectra of Inorganic and Coordination Compounds*, 4th edn., J. Wiley & Sons, New York, 1986.
42 V. Rives-Arnau, G. Munuera and J. M. Criado, *Spectrosc. Lett.*, 1979, **12**, 733.
43 J. M. Fernández, C. Barriga, M. A. Ulibarri, F. M. Labajos and V. Rives, *Chem. Mater.*, 1997, **9**, 312.
44 V. Rives, M. A. Ulibarri and A. Montero, *Appl. Clay Sci.*, 1995, **10**, 83.
45 K. S. W. Sing, D. H. Everett, R. A. W. Haul, L. Moscou, R. Pierotti, J. Rouquerol and T. Sieminiewska, *Pure Appl. Chem.*, 1985, **57**, 603.
46 B. C. Lippens and J. H. de Boer, *J. Catal.*, 1965, **4**, 319.
47 S. J. Gregg, *J. Chem. Soc., Chem. Commun.*, 1975, 699.
48 F. Trifirò, A. Vaccari and O. Clause, *Catal. Today*, 1994, **21**, 185.
49 E. D. Rodghierd, J. Chisaki and E. P. Ciannelis, *Chem. Mater.*, 1997, **9**, 478.
50 J. Hanuza, B. Jezowska-Trzebiatowska and W. Oganowski, *J. Mol. Catal.*, 1985, **29**, 109.
51 F. M. Labajos, V. Rives and M. A. Ulibarri, in *Multifunctional Mesoporous Inorganic Solids*, NATO-ASI, ed. C. A. C. Sequeira and M. J. Hudson, Kluwer, Amsterdam, 1993, p. 207.
52 S. Kannan, A. Narayanan and C. S. Swamy, *J. Mater. Sci.*, 1996, **31**, 2353.

Paper 8/08544G